An immersed boundary method for numerical simulations of boundary layers with roughness

By O. Marxen AND G. Iaccarino

1. Motivation and objectives

Laminar-turbulent transition in compressible, high-speed boundary layers is currently not well understood. This is true for both transition in the absence of intentional forcing as well as for cases where transition is triggered by means of e.g. roughness elements. The latter case is relevant for a number of applications, including the heat-shield of vehicles (re-)entering a planetary atmosphere and the inlet to scramjet combustors for hypersonic cruise vehicles. While transition is undesired on the heat shield due to an associated increase in temperature, it is desirable for scramjets to ensure proper mixing within the combustor. In any case, prediction of the transition location is essential for vehicle design in both types of applications, and a necessary condition for an accurate prediction is an understanding of the physical mechanisms involved.

However, even the first stage of the transition process, that is, amplification of small linear perturbations is not yet well understood for smooth surfaces. Our understanding is even less comprehensive if a localized two- or three-dimensional roughness element is present inside the boundary layer. High-speed, compressible laminar boundary layers often exhibit qualitatively different phenomena than low-speed, incompressible ones, such as shocks and multiple instability modes (Mack 1975). To improve our understanding of the physical mechanisms, appropriate simulation tools are necessary to capture the phenomena associated with compressible boundary layers. In particular, stability investigations such as e.g. Pagella *et al.* (2004) for 2-d or Groskopf *et al.* (2008) for 3-d mean flows require an accurate representation of the respective mean flows.

Only a few fundamental investigations concerning the effect of roughness on instability and transition have been carried out in high-speed flow (e.g. Balakumar 2003). Roughness can be classified as distributed or localized, an overview on both types is given in Schneider (2007) for compressible transitional flow. We only consider a localized roughness here, a type recently reviewed in Berry & Horvath (2007).

Different options are available to represent roughness within a numerical simulation, for instance via artificial boundary conditions (see discussion in Jiménez 2004). For discrete roughness elements, body-fitted methods and immersed boundary methods are both attractive. While the body-fitted method possesses the advantage of a lower computational effort for two-dimensional roughness elements, it will become considerably more demanding for three-dimensional geometries. Moreover, the generation of grids without skewed elements becomes a demanding problem for simulations of a three-dimensional roughness using the body-fitted approach.

The objective of this report is to demonstrate that results from simulations using the immersed boundary method match those using a body-fitted grid for both two- and three-dimensional roughness in a steady-state laminar boundary layer. For a two-dimensional roughness element such a comparison will also be carried out with regard to the evolution of a small-amplitude disturbance wave inside the boundary layer.

2. Governing equations

The flow is governed by the time-dependent 3-d compressible Navier-Stokes equations. These equations are formulated for a calorically perfect gas, an extension to include high-temperature gas effects have been reported in Marxen *et al.* (2007). Non-dimensionalization is based on the free-stream conditions (marked by $_\infty$): a reference temperature $\tilde{T}_{ref} = (\gamma_\infty - 1)\tilde{T}_\infty$, density $\tilde{\rho}_\infty$, specific heat ratio $\gamma_\infty = \tilde{c}_{p,\infty}/\tilde{c}_{v,\infty}$, the speed of sound $\tilde{c}_\infty$, thermal conductivity $\tilde{k}_\infty$, viscosity $\tilde{\mu}_\infty$, and a reference length $\tilde{L}_{ref}$ (all dimensional quantities are marked by $\tilde{}$). This results in the following set of equations for mass, momentum and energy conservation (in non-dimensional form):

$$\frac{\partial \rho}{\partial t} + \frac{\partial}{\partial x_j}\left(\rho u_j\right) = 0, \tag{2.1}$$

$$\frac{\partial \rho u_i}{\partial t} + \frac{\partial}{\partial x_j}\left(\rho u_i u_j + p\delta_{ij}\right) = \frac{\partial \sigma_{ij}}{\partial x_j}, \quad i = 1,2,3, \tag{2.2}$$

$$\frac{\partial E}{\partial t} + \frac{\partial}{\partial x_j}\left[\left(E + p\right) u_j\right] = -\frac{\partial q_{ij}}{\partial x_j} + \frac{\partial}{\partial x_k}\left(u_j \sigma_{ij}\right). \tag{2.3}$$

with the total energy E, the viscous stress tensor σ_{ij} and the heat flux vector q_j:

$$E = e\rho + \frac{1}{2}\rho u_i u_i, \tag{2.4}$$

$$\sigma_{ij} = \frac{\mu}{Re_\infty}\left(\frac{\partial u_i}{\partial x_j} + \frac{\partial u_j}{\partial x_i} - \frac{2}{3}\frac{\partial u_k}{\partial x_k}\delta_{ij}\right), \tag{2.5}$$

$$q_j = \frac{-1}{Re_\infty Pr_\infty Ec_\infty} \times k_e \frac{\partial T}{\partial x_j} - \frac{1}{Re_\infty} \times b_e \frac{1}{\rho}\frac{\partial p}{\partial x_j}. \tag{2.6}$$

The Reynolds number Re_∞, Prandtl number Pr_∞, and Eckert number Ec_∞ are:

$$Re_\infty = \tilde{\rho}_\infty \tilde{c}_\infty \tilde{L}_{ref}/\tilde{\mu}_\infty, \quad Pr_\infty = \tilde{\mu}_\infty \tilde{c}_{p,\infty}/\tilde{k}_\infty, \tag{2.7}$$

$$Ec_\infty = \tilde{c}_\infty^2 / \left(\tilde{c}_{p,\infty}\left(\gamma_\infty - 1\right)\tilde{T}_\infty\right). \tag{2.8}$$

The Mach number M_∞ is computed with the streamwise velocity in the free-stream $\tilde{u}_\infty$ and the speed of sound $\tilde{c}_\infty$, i.e. $M_\infty = \tilde{u}_\infty/\tilde{c}_\infty$. The system of equations is closed by an equation of state:

$$p = R/Ec_\infty \times \rho T. \tag{2.9}$$

In this equation, $R = \tilde{R}/\tilde{c}_{p,\infty}$ is the gas constant:

$$R = \left(\gamma_\infty - 1\right)/\gamma_\infty. \tag{2.10}$$

For a calorically perfect gas, the specific heat $c_p \equiv 1$ and $b_e \equiv 0$, while k_e and μ depend on the temperature and are equal $k_e = \mu$, and the latter can be computed from e.g. Sutherland's law:

$$\mu = T^{3/2} \times \frac{1 + \tilde{T}_S/\tilde{T}_\infty}{T + \tilde{T}_S/\tilde{T}_\infty}, \quad \text{with } \tilde{T}_s = 110.4K. \tag{2.11}$$

The internal energy $e = h - p/\rho$ is given by:

$$e = p/\left(\left(\gamma_\infty - 1\right)\rho\right). \tag{2.12}$$

roughness	Re	Pr_∞	Ec_∞	M_∞	$\tilde{T}_\infty$	x_{ifl}	x_{ofl}	y_{bot}	y_{top}	NX	MY	KZ
2-d	10^5	0.71	1	4.8	55.4 K	1.6065	30.1665	0	1.575	800	200	-
3-d	10^5	0.71	1	4.8	55.4 K	10.6065	28.1665	0	1.575	400	200	40

TABLE 1. Overview of simulation parameters, domain size and resolution.

3. Numerical method and geometry

Two different numerical methods have been applied to compute the flow fields. The basis for the first numerical method (below denoted as finite-difference code) is the algorithm described in Nagarajan *et al.* (2003). Solutions to the compressible Navier-Stokes equations are obtained, applying sixth-order compact finite-differences together with third order explicit Runge-Kutta time stepping. The numerical discretization is constructed on a structured, curvilinear grid using staggered variables. No explicit shock-capturing scheme is present as occurring shocks are very weak and could be treated by applying a high-order compact numerical filter.

The second method, below denoted as finite-volume code, is a commercial computational fluid dynamics solver (FLUENT, ANSYS, Inc. 2008), applying a Roe Riemann solver and a 2nd order TVD scheme. This code uses a second-order accurate finite volume scheme to discretize the governing equations on an unstructured grid.

3.1. *Discretization, integration domains, and boundary conditions*

Free-stream parameters and the size of the integration domain are the same as in Marxen & Iaccarino (2008) and are given in Table 1. The origin of the coordinate system is located at the leading edge of the flat plate, with the inflow of the computational domain placed downstream of the leading edge. The grid is uniformly spaced in streamwise direction x (NX points) and, for the 3-d roughness, also in the periodic spanwise direction z (KZ points). In wall-normal direction, a grid stretching is applied according to the following formula, with κ=0.15 (flat plate and immersed boundary method) or κ=0.25 (body-fitted) and m=1 ... MY:

$$y@(1,m) = y_1 \left((1-\kappa) \left(\frac{m-1}{MY-1} \right)^3 + \kappa \frac{m-1}{MY-1} \right) \tag{3.1}$$

At the inflow x_{ifl}, a self-similar solution is prescribed while the wall boundary condition (B.C.) at y_{bot} is adiabatic with a no-slip condition. In the vicinity of the outflow and in the free-stream, the solution is damped towards the laminar self-similar solution.

3.2. *Geometry and representation of the roughness element*

3.2.1. *Shape of the roughness*

The shape of the roughness is defined by the following analytical function:

$$y_w(x,z) = \frac{h_z}{2} \times \sum_{k=-1}^{+1} k \times (\tanh(s_R \times (x - x_{0,k})) + 1) \text{ with } x_{0,k} = x_{c,R} - \frac{k}{2} \times L_R \,. \tag{3.2}$$

where y_w specifies the distance from the plate surface. The coefficients appearing in this equation are specified in Table 2. While for the 2-d roughness $h_z \equiv h_R$, it is a function of z for the 3-d roughness:

$$h_z(z) = h_R/4 \cdot (\tanh(s_R\,(z + L_R/2)) - \tanh(s_R\,(z - L_R/2))) \,. \tag{3.3}$$

h_R	L_R	s_R	$x_{c,R}$	α_S	β_S	ϱ_1^2	ϱ_2^2	ϱ_3^2
0.1	0.4	20.0	15.0	10^5	$5 \cdot 10^3$	$1 \cdot 10^{-4}$	$5 \cdot 10^{-5}$	$1 \cdot 10^{-4}$

TABLE 2. Coefficients to define the shape of the roughness and parameters used in the immersed boundary method.

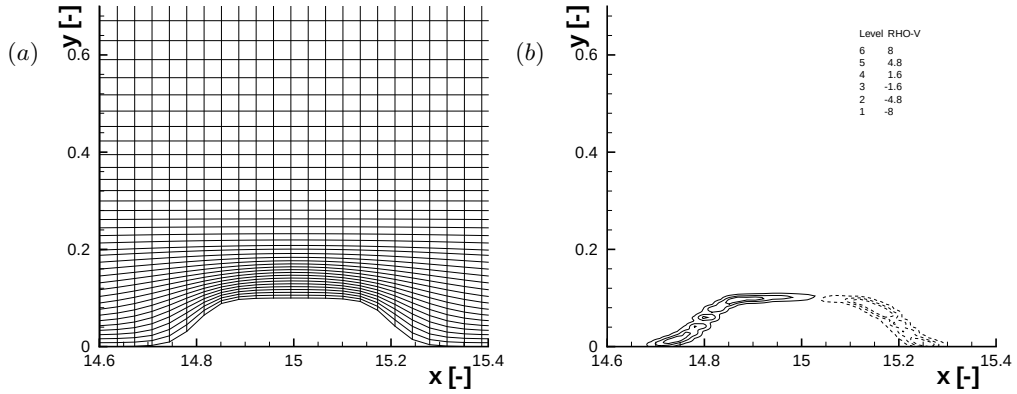

FIGURE 1. (a) Visualization of the grid in the vicinity of the roughness element for the simulations with a body-fitted grid (used for both, the finite-difference and the finite-volume code). Only every 2nd grid point in x and every 4th grid point in y is shown. (b) Contours of the body force in the y momentum equation ("RHO-V") for the simulation with an immersed boundary method. Contours with negative values are given as dashed lines.

3.2.2. *Body-fitted grid*

The first (wall-parallel) grid line $m = 1$ collapses with the wall, i.e. it follows $y_w(x, z)$. In streamwise direction, it is subdivided with an equidistant spacing. The second and the following grid lines ($m > 1$) are computed in a similar way as the first line, but with parameters h_z, s_R, L_R in eqs. (3.2), (3.3) being varied over m. The resulting grid is non-orthogonal, a visualization is given in Fig. 1.

3.2.3. *Immersed boundary method*

Volume forcing is incorporated in the code for the use as an immersed boundary method (IBM), following an approached described in Refs. Mittal & Iaccarino (2005); Wörner *et al.* (2003); von Terzi *et al.* (2001). A forcing term is added to the right-hand side of the momentum eqs. (2.2) ($\mathbf{x} = (x \;\; y \;\; z)^T = (x_1 \;\; x_2 \;\; x_3)^T$) as:

$$B_i(\mathbf{x}, t) = \rho \oint_S b_i\left(\mathbf{x}_S\right) \times g\left(\mathbf{x} - \mathbf{x}_S\right) dS\,, \tag{3.4}$$

$$\text{with } b_i(\mathbf{x}_S, t) = \alpha_S \times \int_0^t u_i\left(\mathbf{x}_S, t'\right) dt' + \beta_S \times u_i\left(\mathbf{x}_S, t\right) \tag{3.5}$$

$$\text{and } g\left(\mathbf{x} - \mathbf{x}_S\right) = \Pi_{i=1\ldots3} \exp\left(-\left((x_i - x_{i,S})/\varrho_i\right)^2\right). \tag{3.6}$$

The coefficients in eqs. (3.4) to (3.6) are given in Table 2. The determination of all the geometrical information required to enforce the immersed boundary is carried out in a pre-processing step. The wall-normal distribution of grid points for all x locations is identical to the inflow, i.e. $y@(n, m) = y_@(1, m)$.

$x_{c,strip}$	L_{strip}	ω	A_v	$Re_{x_{c,strip}}$
5.49	4.203	48	$2 \cdot 10^{-4}$	741

TABLE 3. Forcing parameters for the simulations of disturbance evolution (2-d roughness only).

3.3. *Disturbance forcing*

For the case of a two-dimensional roughness, disturbances of a certain frequency are forced via blowing and suction at the wall upstream of the roughness element. The non-dimensional forcing frequency ω is defined as ($\tilde{f}$ is the dimensional frequency):

$$\omega = F \cdot M_\infty \cdot Re^*, \quad \text{with } F = 2\pi \tilde{f} \tilde{\mu}_\infty \tilde{u}_\infty^{-2} \tilde{\rho}_\infty^{-1}. \tag{3.7}$$

The boundary condition at the wall (subscript $_w$) reads (for parameters see Table 3):

$$(\rho v)_w = A_v \cdot \sin(\omega t) \cdot \sin(16\,\xi) \cdot e^{-\sqrt{2}/2\xi^2} \quad \text{with} \quad \xi = (x - x_{c,strip})/L_{strip}\,. \tag{3.8}$$

To analyze the instability of the boundary layer, results are Fourier analyzed in time with a fundamental circular frequency $\Omega = \omega/2$, i.e. with half the forcing frequency of the respective case. The inverse discrete Fourier transform for $s = u_i, \rho, T, p$ is:

$$s(\mathbf{x}, t_l) = \frac{1}{LP} \sum_{h=0}^{H} |\hat{s}_h(\mathbf{x})| \cdot \cos[2\,h\,\Omega\,l\Delta t + \Phi_h(\mathbf{x})], \;\; l = [0, LP-1], \tag{3.9}$$

where LP is the sample size in two forcing periods, l the sampling index and Δt the sampling interval so that the discrete time $t_l = l\Delta t$. The computations are advanced up to 94 forcing periods before carrying out the Fourier analysis for two consecutive forcing periods.

The streamwise disturbance amplification is quantified using wall-normal maxima of the amplitudes of a disturbance quantity $\hat{s}$, which are computed as

$$\hat{s}_{harm}^{max}(x) = \max\{|\hat{s}_{harm}(x = const, y)|\}. \tag{3.10}$$

In the following we use a local Reynolds number $Re_x{=}R_x{=}\sqrt{x \cdot Re}$.

3.4. *Verification*

To assess the accuracy of the finite-difference code regarding the growth of small disturbances, disturbance evolution in a flat plate boundary layer at Mach 4.8 has been simulated and compared to results obtained by other authors, details are given in Marxen *et al.* (2007). For the case with two-dimensional roughness, a grid study has been performed (for the body-fitted grid, finite-difference code), showing convergence for both the mean and disturbance quantities (Marxen & Iaccarino 2008).

4. Mean flow

The ratio between the boundary-layer thickness based on $u/u_\infty{=}0.99$ for the flat-plate at the location of the roughness ($x = 15$) and the height of the roughness is ≈ 0.55.

4.1. *Two-dimensional roughness*

The localized roughness element leads to boundary-layer separation both upstream and downstream of it. A small amount of reverse flow is visible in wall-normal profiles of the streamwise velocity (Fig. 2).

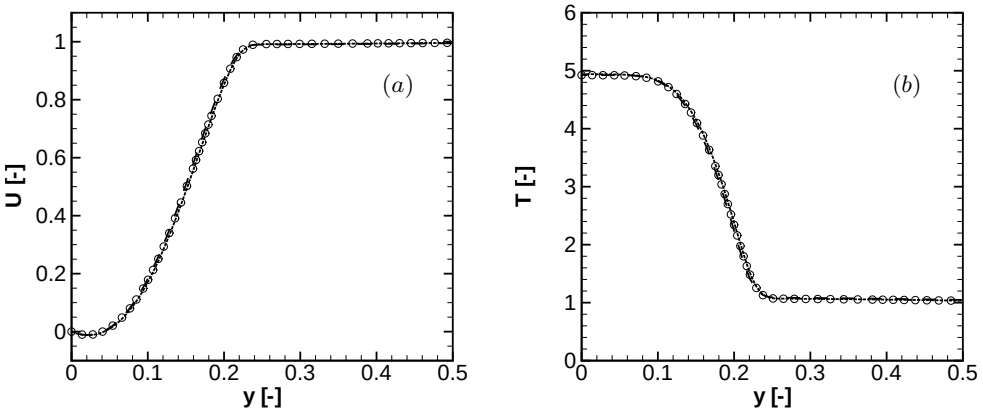

FIGURE 2. Mean flow profiles upstream of the two-dimensional roughness at x=14.4 (Re_x=1200), normalized with free-stream values. Symbols: body-fitted grid, finite-difference code. Dotted lines: immersed-boundary method, finite-difference code. Dashed lines: body-fitted grid, finite-volume code. (a) streamwise velocity and (b) temperature.

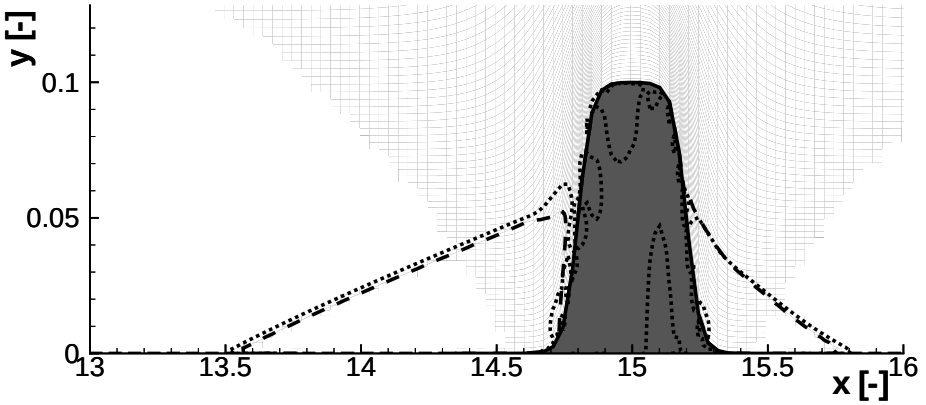

FIGURE 3. Contours of vanishing streamwise velocity, two-dimensional roughness (dashed for body-fitted, dotted for the immersed-boundary method, both obtained with the finite-difference code). The wall-normal axis is enlarged by a factor of 10 compared to the streamwise axis.

The length of the separation bubbles upstream and downstream differ roughly by a factor of two: its length is approximately $13h_R$ upstream of the roughness and $6h_R$ downstream of it (Fig. 3). This observation is consistent with reports of Balakumar (2003) for a boundary layer at Mach 3.5: "... for $h/\delta = 1/2$, the upstream separated region is about $15h$ and the downstream region is about $8h$."

The agreement between the three different calculation methods using a body-fitted grid and an immersed boundary method is very good (Fig. 2 and 3). This holds true even for mean-flow profiles on top of the roughness element (Fig. 4) and downstream of it (Fig. 5).

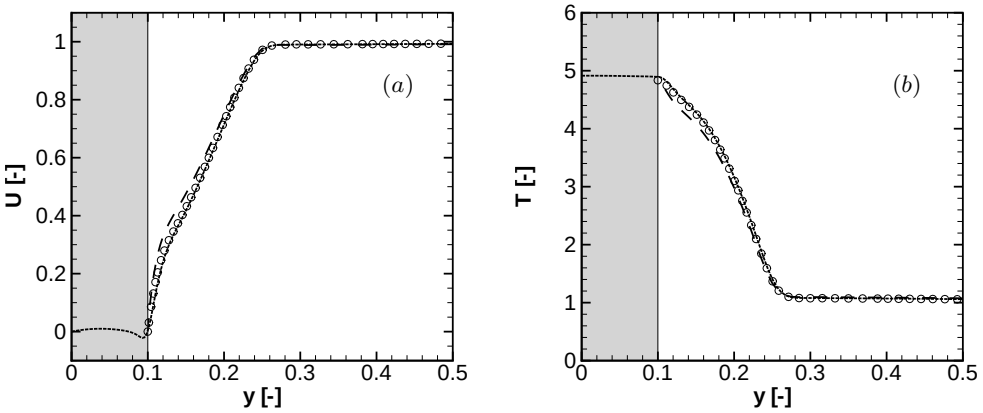

FIGURE 4. Same as Fig. 2, but at the center of the two-dimensional roughness at x=15.0 (Re_x=1225). The grey area marks locations inside the roughness.

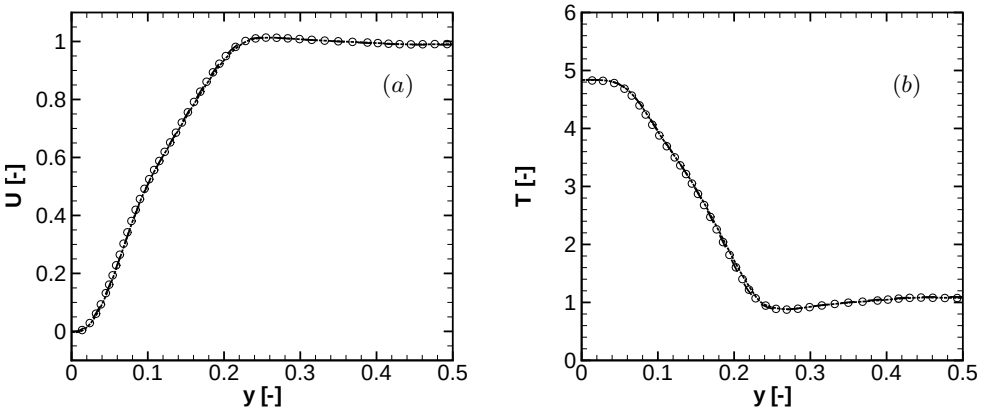

FIGURE 5. Same as Fig. 2, but downstream of the two-dimensional roughness at x=15.625 (Re_x=1250).

4.2. *Comparison between two- and three-dimensional roughness*

To highlight the qualitatively different features of the flow with the two-dimensional and the three-dimensional roughness, representations of the mean flow fields are given in Fig. 6 and Fig. 7, respectively. In both cases, the roughness element causes a compression followed by an expansion, which again is followed by a compression. For the two-dimensional roughness however, only the final compression causes a weak oblique shock, visible downstream of the roughness element. In case of the three-dimensional roughness, also the first compression induces a shock. The reason for this difference lies in the different sizes of the separation zones. The separation bubble in front of the two-dimensional roughness is considerably larger, causing a more gradual increase in pressure without abrupt change in flow direction. In the case with a three dimensional roughness, the separation region downstream of the roughness is longer, but limited to the region behind the center of the roughness (Fig. 8). For the case with a three-dimensional roughness, the shock regions

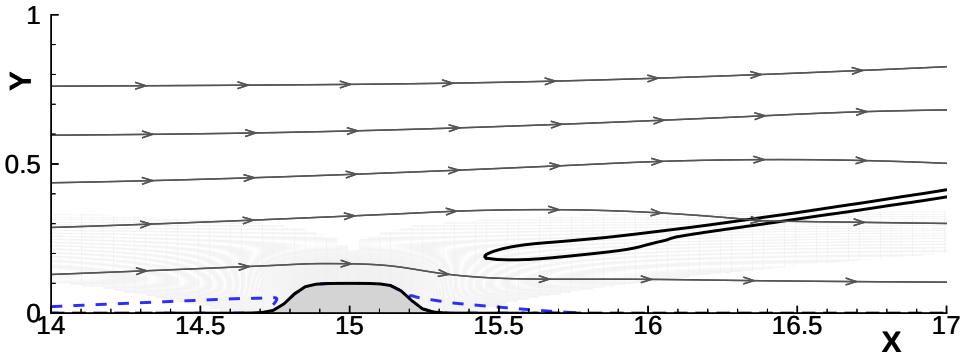

FIGURE 6. Contours of the streamwise density gradient $\partial\rho/\partial x = 0.4$ (solid) together with contours of vanishing streamwise velocity (dashed) and selected streamlines (lines with arrows), two-dimensional roughness.

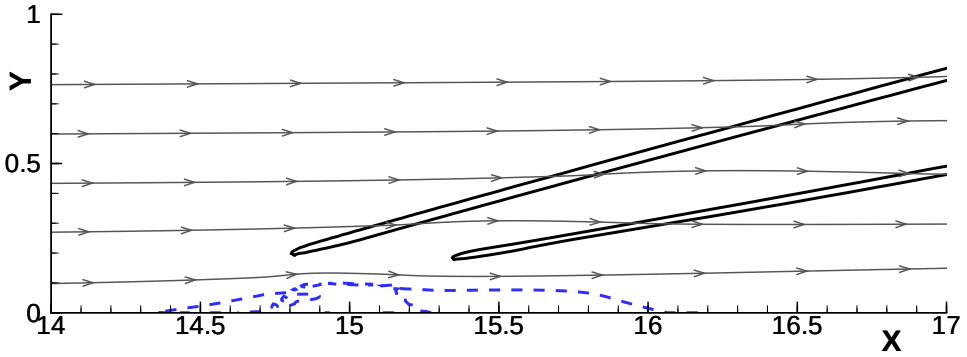

FIGURE 7. Contours of the streamwise density gradient $\partial\rho/\partial x = 0.4$ (solid) together with contours of vanishing streamwise velocity (dashed) and selected streamlines (lines with arrows) in the center plane $z = 0$ of the three-dimensional roughness, immersed-boundary method.

are mostly confined to the spanwise planes which cut the roughness (Fig. 8).

A comparison of mean-flow profiles on top of the three-dimensional roughness between the immersed boundary-method and the body-fitted grid (Fig. 9) is similarly good as before for the two-dimensional roughness. Downstream of the roughness, a pair of streamwise vortices (not shown, but see Groskopf *et al.* 2008) causes a region of low speed but high temperature (Fig. 10, in the interval $y \approx [0.05, 0.15]$). A comparison between the immersed-boundary and the body-fitted method of profiles of different flow quantities at a fixed streamwise plane is given in Fig. 11. Although not exactly equivalent as in the case with a 2-d roughness, in particular for off-center locations, the results possess very similar features.

5. Disturbance evolution in the flow with a 2-d roughness element

Discrete roughness elements in high-speed boundary layers are expected to profoundly alter the instability of the boundary layer. In particular, separation regions, which here develop upstream and downstream of the obstacle as shown in the previous section, are known to increase convective disturbance amplification. Pagella *et al.* (2004) could show

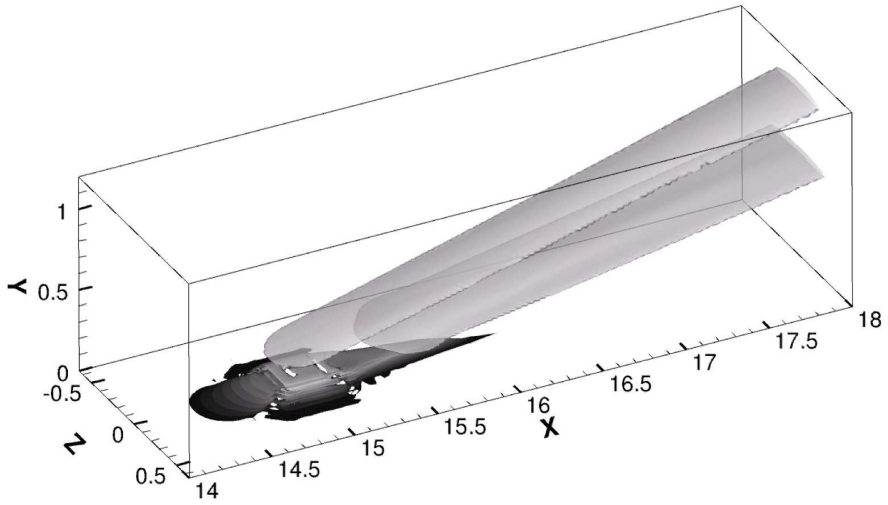

FIGURE 8. Isosurfaces of the streamwise density gradient $\partial\rho/\partial x = 0.4$ (light grey) for the three-dimensional roughness together with isosurfaces of vanishing streamwise velocity, the latter appear in darker grey being grey-scale colored by the distance from the wall ($y = 0 \ldots 0.1$).

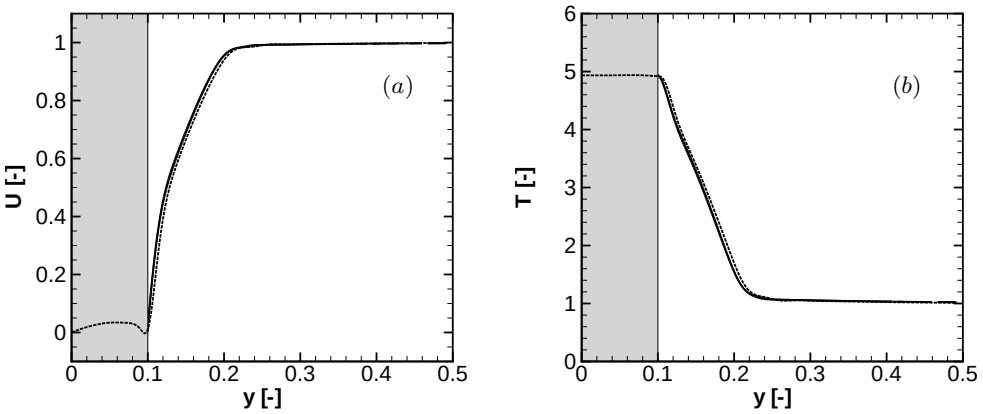

FIGURE 9. Mean flow profiles at the center of the three-dimensional roughness at x=15 (Re_x=1225), z=0, normalized with free-stream values. The grey area marks locations inside the roughness. Dotted lines: immersed-boundary method, finite-difference code. Solid lines: body–fitted grid, finite-volume code. (a) streamwise velocity and (b) temperature.

this for the case of shock-boundary-layer interaction and ramp flow. Such a recirculation zone might even lead to an absolute or global instability (Robinet 2007).

Here, we concentrate on convective amplification, as no evidence for an absolute instability was found: a steady-state solution was easily attainable. We have carried out a variety of simulations with upstream disturbance forcing of several frequencies. However, in the present paper it is sufficient to consider only a single disturbance frequency; the objective of this analysis is to compare disturbance amplification obtained from simulations with the body-fitted and the immersed-boundary method.

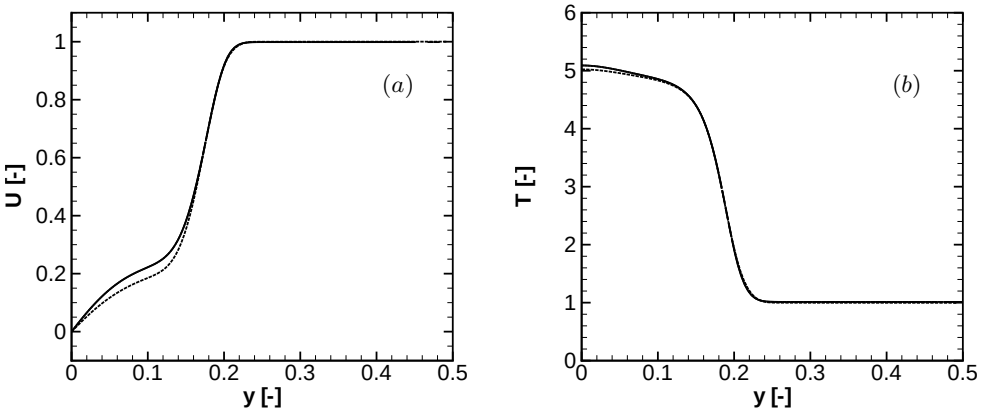

FIGURE 10. Same as Fig. 9, but downstream of the three-dimensional roughness at x=18 (Re_x=1342), z=0.

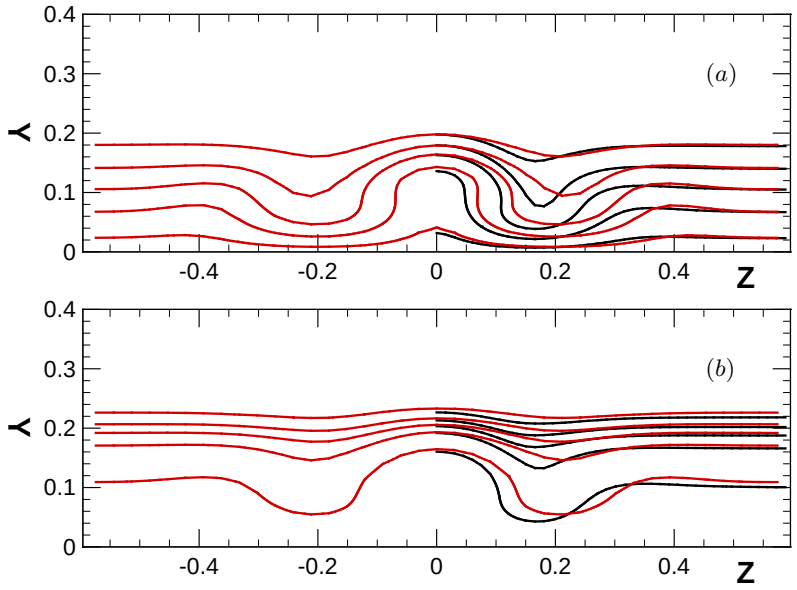

FIGURE 11. Contours of flow variables from simulation of body fitted (dark/black) and immersed boundary method (grey/red) for the three-dimensional roughness at $x = 18$. (a) u=0.1 . . . 0.9, Δ=0.2, (b) ρ=0.25 . . . 0.95, Δ=0.125.

5.1. *Disturbance flow*

The choice of the disturbance frequency was guided by results reported in Pagella *et al.* (2002). For a flat plate without roughness the disturbance at the chosen frequency is, according to Mack (1975)'s classification, an amplified first-mode instability up to $Re_x \approx$ 1350 and becomes an amplified second mode downstream of $Re_x \approx 1500$.

Comparing disturbance amplification with and without roughness element, we see that the disturbance amplitude increases beyond values for the flat plate upstream and downstream of the roughness element (Fig. 12). It is, however, beyond the scope of this report

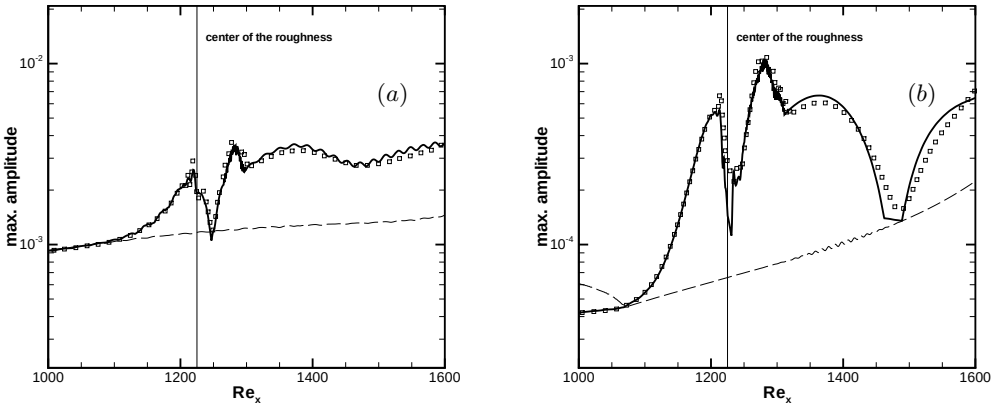

FIGURE 12. Streamwise evolution of maximum disturbance component with roughness element. The roughness element is centered at x=15 (Re_x=1225) and marked by a line. Symbols: body–fitted grid. Thick lines: immersed-boundary method. Dashed (thin) lines: flat plate. (a) density $\hat{\rho}_1^{max}$ and (b) wall-normal velocity component $\hat{v}_1^{max}$.

to discuss the details of the disturbance evolution. Instead, we note that the agreement between results using a body-fitted grid and an immersed boundary method is, again, favorable. This holds true not only with respect to the observed alternation of growth and decay behind the roughness (Fig. 12) but also for wall-normal amplitude and phase functions (see Marxen & Iaccarino 2008).

6. Conclusions

The interaction of a localized two- and three-dimensional roughness with a Mach 4.8 boundary layer has been numerically investigated. Two different approaches have been used to represent the roughness: a body-fitted curvilinear grid discretization and an immersed boundary method on a Cartesian grid. The latter method is based on volume forcing. For the former method two entirely different numerical schemes have been applied. An overall good agreement between the various methods is found for the mean flow. For the two-dimensional roughness with a small perturbation in the boundary layer, also disturbance quantities agreed well between the body-fitted and the immersed-boundary method. The immersed boundary method is applicable for the generation of mean flows for subsequent stability investigations and for the computation of the interaction of a roughness with a boundary-layer perturbation.

7. Future work

A detailed analysis of the evolution of the perturbation in the presence of the 2-d roughness element is currently in progress. For the case of the 3-d localized roughness element, a grid study is planned to confirm the results reported here and clarify the observed slight discrepancies between the immersed-boundary method and the body-fitted approach. Once a grid-converged solution is verified, an investigation of disturbance amplification is planned to continue the work reported in Groskopf *et al.* (2008).

Acknowledgments

Financial support from the National Aeronautics and Space Administration (NASA) under award No. NNX07AC29A is gratefully acknowledged. We are grateful to S. Lele and A. Mani for providing the finite-difference code.

REFERENCES

ANSYS, Inc. 2008 FLUENT®: Robust, Reliable, Comprehensive CFD. http://www.fluent.com/software/fluent/modeling_spec.htm.

Balakumar, P. 2003 Transition in a supersonic boundary-layer due to roughness and acoustic disturbances. *AIAA Paper* 2003–3589.

Berry, S. A. & Horvath, T. J. 2007 Discrete Roughness Transition for Hypersonic Flight Vehicles. *AIAA Paper* 2007–0307.

Groskopf, G., Kloker, M. J., Marxen, O. & Iaccarino, G. 2008 BiGlobal Secondary Stability Theory for High-Speed Boundary-Layer Flows. In *Proceedings of the 2008 Summer Program*. Center for Turbulence Research, Stanford University.

Jiménez, J. 2004 Turbulent flows over rough walls. *Annu. Rev. Fluid Mech.* **36**, 173–96.

Mack, L. M. 1975 Linear Stability Theory and the Problem of Supersonic Boundary-Layer Transition. *AIAA J.* **13** (3), 278–2285.

Marxen, O. & Iaccarino, G. 2008 Numerical simulation of the effect of a roughness element on high-speed boundary-layer instability. 38th AIAA Fluid Dynamics Conference and Exhibit, 23-26 June 2008 / Seattle, WA.

Marxen, O., Iaccarino, G. & Shaqfeh, E. S. G. 2007 Numerical simulation of hypersonic instability using different gas models. In *Annual Research Briefs 2007*. Center for Turbulence Research, Stanford University.

Mittal, R. & Iaccarino, G. 2005 Immersed Boundary Methods. *Ann. Rev. Fluid Mech.* **37**, 239–261.

Nagarajan, S., Lele, S. K. & Ferziger, J. H. 2003 A robust high-order method for large eddy simulation. *J. Comput. Phys.* **191**, 392–419.

Pagella, A., Babucke, A. & Rist, U. 2004 Two-dimensional numerical investigations of small-amplitude disturbances in a boundary layer at Ma=4.8: Compression corner versus impinging shock wave. *Phys. Fluids* **16** (7), 2272–2281.

Pagella, A., Rist, U. & Wagner, S. 2002 Numerical investigations of small-amplitude disturbances in a boundary layer with impinging shock wave at Ma=4.8. *Phys. Fluids* **14** (7), 2088–2100.

Robinet, J. C. 2007 Bifurcations in shock-wave/laminar-boundary-layer interaction: global instability approach. *J. Fluid Mech.* **579**, 85–112.

Schneider, S. P. 2007 Effects of Roughness on Hypersonic Boundary-Layer Transition. *AIAA Paper* 2007–0305.

von Terzi, D. A., Linnick, M. N., Seidel, J. & Fasel, H. F. 2001 Immersed Boundary Techniques for High-Order Finite-Difference Methods. 31st AIAA Fluid Dynamics Conference & Exhibit, 11-14 June 2001 / Anaheim, CA.

Wörner, A., Rist, U. & Wagner, S. 2003 . *AIAA J.* **41** (2), 192–197.